J. Appl. Comput. Mech., 11(2) (2025) 382-398
DOI: 10.22055/jacm.2024.46802.4595

ISSN: 2383-4536
jacm.scu.ac.ir

Shahid Chamran
University of Ahvaz

Journal of
Applied and Computational Mechanics

Research Paper

Intervention of the Koo-Kleinstreuer and Li Model in Nanofluid Flow over Magnetic Dipole Centered Curved Sheet and Optimizing Entropy using Response Surface Methodology

K.G. Vidhya, F. Almeida, P. Kumar, B. Nagaraja

Department of Mathematics, School of Engineering, Presidency University, Rajanakunte, Yelahanka Bengaluru-560064, Karnataka, India,
Email: vidhya777nvn@gmail.com (K.G.V.); felcitaalmeida@gmail.com (F.A.); pradimath@gmail.com (P.K.); nagaraj.kalapanahalli@gmail.com (B.N.)

Received May 03 2024; Revised August 02 2024; Accepted for publication August 05 2024.
Corresponding author: B. Nagaraja (nagaraj.kalapanahalli@gmail.com)

Abstract. Nanofluids are recognized as smart fluids, offering significant advantages for enhancing heat and mass transfer. Their utility spans various domains, including electronics, biomedicine, and industrial processes. Against this backdrop, our present study focuses on examining response surface method and carrying out sensitivity analysis for Al_2O_3 nano-fluid flow over a stretching curved geometry. The response surface mechanism is envisioned for Eckert number, Prandtl number, as well as radiation parameter. This study introduces a novel perspective by investigating the interplay of heat and mass transfer in nano-liquids, incorporating radiative heat flux and the influence of a magnetic dipole. The Koo-Kleinstreuer and Li model analyses Brownian motion effect on viscosity and effective thermal conductivity. The modelled problem is solved using the Runge-Kutta-Fehlberg 4th–5th method. The results show that as ferrohydrodynamic interaction intensifies, it leads to an augmentation in velocity near the boundary, followed by a subsequent rise; however, the temperature profile experiences a decrease. As the thermal radiation parameter escalates, so does the temperature profile. Conversely, the concentration profile diminishes with heightened chemical reaction and Schmidt number. Entropy rises in correlation with an enhancement in the temperature ratio parameter, yet the Bejan number declines. The Pareto chart highlights 2 as the critical point for the Eckert number, Prandtl number, and radiation parameter. Specifically, the Prandtl number demonstrates a negative sensitivity across all levels of radiation parameter. Conversely, both the Eckert number and radiation parameter exhibit positive sensitivity at all levels of radiation parameter.

Keywords: Curved stretching sheet; Koo-Kleinstreuer-Li model; Magnetic dipole; Non-linear radiation; Response surface methodology.

1. Introduction

Heat transfer is essential in numerous technical applications and industrial processes, such as cooling aircraft engines, blow molding, and temperature control. For heat transfer devices to be efficient, they should transport a significant amount of thermal energy across a tiny temperature difference. The debate over fossil fuel depletion has underscored the importance of energy consumption. Convection, the transfer of heat through fluids, is a common method studied for enhancing efficiency. Numerous studies have focused on improving heat transfer as well as the efficiency of fluids to expedite the heat transfer in process. Low thermal conductivity is a major factor affecting heat exchanger productivity in manufacturing sectors. Various techniques, however, have limitations. One innovative method involves suspending small hard particles in fluids to rise thermal conductivity by enhancing surface area. Creating a slurry by mixing granules, including non-metallic, metallic, and polyethylene particles, aims to boost thermal conductivity beyond that of normal fluids. While it is expected that aerosols in fluids will exhibit higher thermal conductivity, previous studies on suspensions' thermal conductivity have been limited to mm-scale measures. It is extensively acknowledged that the thermal conductivity of postponements is enhanced by the surface to volume fraction of the tiny particles.

The formulation of nanofluids involves suspending nanoparticles in typical carrier liquids such as oil, ethylene glycol, and argon. Over the last two decades, these nano-liquids have gained widespread attention in scientific circles owing to their expanding applications in diverse fluid systems, including advanced nuclear technologies and the distribution of nanodrugs. Choi and Eastman [1] be located the primary researchers who conducted studies on nanofluids. Hayat et al. [2] investigated the convective flow stream of nanofluid, consisting of water as well as magnetite (Fe_3O_4) nanoparticles, over a curved geometry. Sharma and Bisht [3] investigated the Magneto-hydrodynamic (MHD) flow as well as heat transfer characteristics of nano-fluids (comprising H_2O as the base fluid with either copper or silver nanoparticles) along a nonlinear, curved stretching geometry. Usama et al. [4] conducted research on the stability analysis of nanofluids based on water over a curved geometry. Subsequent to that, various researchers formulated distinct mathematical models [5-7].

Published online: August 09 2024

Koo and Kleinstreuer [8] studied thermal efficiency linked to Brownian movement formulation and nano-particle transmission. Moreover, Li [9] adapted the K-K models to create the KKL model. Several researchers utilized this model to analyze the thermal characteristics of nano liquids on various surfaces. Kandelousi and Sheikholeslami [10] employed the KKL correlation to model the flow along with the thermal transfer of nano-fluid in a permeable channel. Sheikholeslami and Ganji [11] examined the flow of nano liquid between similar plates using the KKL model. Mohammadein et al. [12] conducted a mathematical analysis on how magnetic field along with thermal radiation affects forced-convection fluid flow of CuO-H_2O nano-fluid over an elongated sheet using stagnation point, considering the effects of suction and injection and employing the KKL model. Kumar et al. [13] explored convective thermal transfer and utilized the KKL correlation to simulate nanofluid flow on curved geometry.

In view of numerous applications, a fascinating area for research is the flow of curved stretched sheets in mechanical engineering works, oil sectors, and the polymer industry. Sajid et al. [14] investigated viscous flow with respect to a curved sheet. The micropolar fluid flow with heat radiation on a curved stretching sheet was conscious by Naveed et al. [15]. Sanni et al. [16] investigated the viscous fluid flow of a nonlinear, curved surface. Hayat et al. [17] performed a thorough examination of the micropolar fluid flow through a curved geometry. On the Walter-B fluid across the ferromagnetic flow of a curved stretched sheet, the effects of porosity, heat transmission, and magnetic dipole were investigated by Khan et al. [18] using gyrotactic microbiological motility and cubic autocatalysis chemical processes.

The dipole is a conceptual structure that performs field assessments via a complicated charging mechanism. Usually, a magnetic dipole is generating a constant magnetic field. The evident relationship between a magnetic dipole phenomenon and magnetic field has made it popular tool demonstrating its applications in medicine. Magnetic dipoles offer benefits in NMR spectroscopy and magnetotherapy, showcasing their relevance in these fields. Boyer [19] was the first researcher who studied the magnetic dipole in 1988. Ishak [20] proposed that the effects of linear radiation on the flow past a flat plate can be simplified by modifying the Prandtl number using a factor determined by the radiation parameter. This suggests that the influence of linear radiation on both flow and heat transfer is minimal, both physically and computationally. Zeeshan and Majeed [21] investigated the impact of a magnetic dipole on the fluid flow and thermal transfer characteristics of a Jeffrey fluid over a stretching surface, highlighting the changes in temperature and velocity due to ferromagnetic effects. Usman et al. [22] explored the thermal and mass transfer properties over a curved sheet in the presence of ferrofluid, a magnetic dipole, and a chemical reaction. Kumar et al. [23] analyzed the influence of a magnetic dipole on the transient flow of a Casson-Williamson nanofluid over an extended, slippery, curved melting sheet.

Considering this perspective, some recent studies have introduced the concept of radiative (nonlinear) heat transfer. It is observed that in the situation of non-linear radiation, the energy equation becomes markedly non-linear and incorporates an extra temperature representing the ratio of wall temperature to atmospheric temperature. Hayat et al. [24] explored the MHD flow of nano-liquids in the presence of thermal (nonlinear) radiation. Hayat et al. [25] investigated the magnetohydrodynamic (MHD) flow induced by a curved stretching sheet, incorporating the effects of thermal radiation and chemical reactions. Patel and Singh [26] explored the micropolar fluid flow with non-linear thermal radiation over a curved surface. Muhammad et al. [27] examined the Newtonian heating of a hybrid nanofluid on a curved geometry, taking into account the effect of viscous dissipation.

The available literature comprehensively covers the investigation and modelling of nanofluid over various surfaces, with special emphasis on analysing the Koo-Kleinstreuer and Li (KKL) model in a variety of situations. This article uses the response surface approach to determine the parametric effect on entropy in order to get an optimized system. Additionally, a sensitivity analysis is performed and also investigates the flow, thermal, and mass transfer of nanofluids (Al_2O_3-H_2O) using the KKL model on a curved surface, incorporating magnetic dipole effects, radiative (non-linear) heat flux, chemical reaction, convective, and slip boundary conditions. The solution approach involves the utilization of the RKF 4th-5th order technique through the shooting method for solving the reduced ODE. Furthermore, the article visually presents fluctuations in velocity, thermal, and concentration gradients.

2. Mathematical Formulation

In the modelling, a steady, 2-D fluid flow is analyzed over a stretching, curved sheet with a nano-liquid containing Al_2O_3 nanoparticles and H_2O as the carrier fluid. The simulation involves correlating the KKL nanofluid model to analyze further aspects such as flow, effective thermal conductivity. In Fig. 1, the surface is raised along the semicircle of radius R by applying two equal and opposite strength in s-direction while maintaining the fixed position of the origin and having r-direction perpendicular to it. B_0 is the magnetic field strength parallel to r direction applied to the sheet. The governing equations for the curved extending sheet, where stretching velocity is represented as $U_w(s)=\breve{a}s$ with a stretching constant $\breve{a}$, are expressed in (r,s) curvilinear coordinates. Magnetic dipole, non-linear radiative heat flux, chemical reaction, Joule dissipation, slip and convective boundary conditions are accounted in the modelling of physical phenomena.

Governing equations for the current mathematical model are as follows, based on the aforementioned assumptions [28]:

$$\frac{\partial}{\partial r}\{(R+r)v\}+R\frac{\partial u}{\partial s}=0, \tag{1}$$

$$\frac{1}{R+r}u^2=\frac{1}{\rho_{nf}}\frac{\partial p}{\partial r}, \tag{2}$$

$$v\frac{\partial u}{\partial r}+\frac{R}{R+r}u\frac{\partial u}{\partial s}+\frac{uv}{R+r}=-\frac{1}{\rho_{nf}}\frac{R}{R+r}\frac{\partial p}{\partial s}+\nu_{nf}\left(\frac{\partial^2 u}{\partial r^2}+\frac{1}{R+r}\frac{\partial u}{\partial r}-\frac{1}{(R+r)^2}u\right)+\frac{\mu_0 M}{\rho_{nf}}\frac{\partial H}{\partial s}, \tag{3}$$

$$u\frac{R}{R+r}\frac{\partial T}{\partial s}+v\frac{\partial T}{\partial r}=\frac{k_{nf}}{(\rho Cp)_{nf}}\left(\frac{1}{R+r}\frac{\partial T}{\partial r}+\frac{\partial^2 T}{\partial r^2}\right)-\frac{1}{(\rho Cp)_{nf}(R+r)}\frac{\partial}{\partial r}(R+r)q_r+\frac{1}{(\rho Cp)_{nf}}\left(u\frac{\partial H}{\partial s}+v\frac{\partial H}{\partial r}\right)\mu_0 T\frac{\partial M}{\partial T}+\frac{\mu_{nf}}{(\rho Cp)_{nf}}\left(\frac{\partial u}{\partial r}+\frac{u}{R+r}\right)^2, \tag{4}$$

$$v\frac{\partial C}{\partial r}+\frac{R}{R+r}u\frac{\partial C}{\partial s}=D_m\left(\frac{\partial^2 C}{\partial r^2}+\frac{1}{R+r}\frac{\partial C}{\partial r}\right)-k_r(C-C_\infty). \tag{5}$$

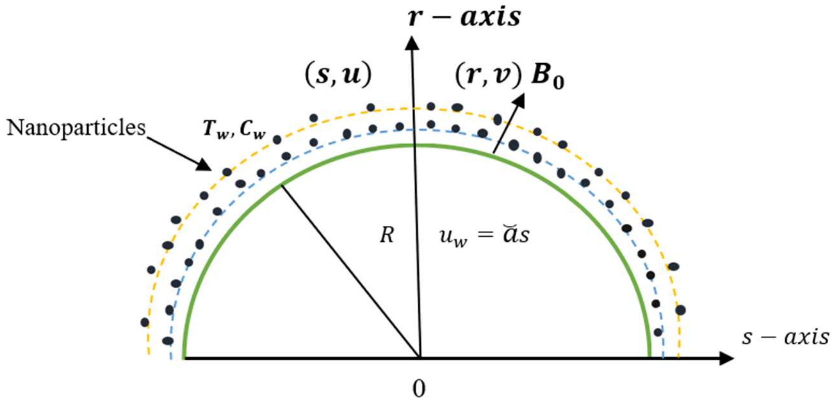

Fig. 1. The geometry of the flow problem.

Boundary conditions are [29]:

$$\begin{gathered} u = \breve{a}s + \lambda_1\left(\frac{\partial u}{\partial r} - \frac{u}{R+r}\right) + \lambda_2\left(\frac{\partial^2 u}{\partial r^2} + \frac{1}{R+r}\frac{\partial u}{\partial r} - \frac{u}{(R+r)^2}\right),\ v = 0, \\ -k_{nf}\frac{\partial T}{\partial r} = h_t(T_w - T),\ -D_m\frac{\partial C}{\partial r} = k_c(C_w - C),\ \text{at } r = 0, \\ u \to 0,\ v \to 0,\ \frac{\partial u}{\partial r} \to 0,\ \ T \to T_\infty,\ \ C \to C_\infty,\ \text{as } r \to \infty, \end{gathered} \tag{6}$$

where (u,v) are velocity components along (s,r) directions, respectively, ρ - density, ν - kinematic viscosity, p - pressure, k - thermal conductivity, μ_0 - magnetic permeability, T - temperature, M - magnetization, C - concentration, μ - dynamic viscosity, H - magnetic field, D_m - diffusion coefficient, k_r - chemical reaction rate, λ_1 - first order slip, Cp - specific heat capacity, λ_2 - second order slip, h_t - convective heat transfer co-efficient, k_c - convective mass transfer coefficient. The subscripts nf and f denotes nanofluid and fluid respectively. The approximation defines the radiative heat flux [24]:

$$q_r = -\frac{4\sigma^*}{3k^*}\frac{\partial T^4}{\partial r} = -\frac{16\sigma^*}{3k^*}T^3\frac{\partial T}{\partial r}, \tag{7}$$

where k^* - mean absorption coefficient and σ^* - Stefan-Boltzmann constant. Thus, energy equation becomes:

$$v\frac{\partial T}{\partial r} + \frac{R}{R+r}u\frac{\partial T}{\partial s} = \frac{k_{nf}}{(\rho Cp)_{nf}}\left(\frac{\partial^2 T}{\partial r^2} + \frac{1}{R+r}\frac{\partial T}{\partial r}\right) - \frac{1}{(\rho Cp)_{nf}(R+r)}\frac{\partial}{\partial r}\left(-\frac{16\sigma^*}{3k^*}T^3\frac{\partial T}{\partial r}\right) + \frac{1}{(\rho Cp)_{nf}}\left(u\frac{\partial H}{\partial s} + v\frac{\partial H}{\partial r}\right)\mu_0 T\frac{\partial M}{\partial T} + \frac{\mu_{nf}}{(\rho Cp)_{nf}}\left(\frac{\partial u}{\partial r} + \frac{u}{R+r}\right)^2, \tag{8}$$

- Magnetic Dipole: The magnetic field at the source experiences the following effects on the liquid stream due to scalar strength Φ and apparent magnetic dipole [23]:

$$\Phi = \frac{\gamma}{2\pi}\left\{\frac{s}{s^2 + (r+g)^2}\right\}, \tag{9}$$

The magnetic fields (H_r) and (H_s) have the following characteristics: g indicates the distance across dipoles, and γ signifies the magnetic field strength on the source:

$$H_r = -\frac{\partial \Phi}{\partial r} = \frac{\gamma}{2\pi}\frac{2s(r+g)}{\left\{s^2 + (r+g)^2)\right\}^2}, \tag{10}$$

$$H_s = -\frac{\partial \Phi}{\partial s} = \frac{\gamma}{2\pi}\frac{s^2 - (r+g)}{\left\{s^2 + (r+g)^2)\right\}^2}. \tag{11}$$

The established relation indicates direct variation between the magnetic force and quantity of H:

$$H = \sqrt{H_r^{\,2} + H_s^{\,2}}. \tag{12}$$

The linear estimation of temperature (T) can be derived from the (M) magnetization, as illustrated down:

$$M = K_1(T - T_\infty),$$

where K_1 is ferromagnetic co-efficient.

- Thermophysical characteristics: Thermo-physical properties of nanoparticles and base fluid are presented in Table 1 and we have:

- Density: $\rho_{nf} = \rho_f(1-\varphi) + \varphi\rho_s$,
- Heat capacitance: $(\rho Cp)_{nf} = (1-\varphi)(\rho Cp)_f + \varphi(\rho Cp)_s$.

Table 1. Thermo-physical properties of nanoparticles and base fluid [30].

Physical properties	Cp (J/kgK)	k (W/mK)	ρ (kg/m^3)	Dp (nm)
Water (H_2O)	4179	0.613	997.1	-
Alumina (Al_2O_3)	765	40	3970	47

Table 2. Co-efficient values of Al_2O_3-Water nanofluid [30].

Co-efficient values	Al_2O_3-Water
a_1	52.813488759
a_2	6.115637295
a_3	0.6955745084
a_4	$4.17455552786 \times 10^{-02}$
a_5	0.176919300241
a_6	-298.19819084
a_7	-34.532716906
a_8	-3.9225289283
a_9	-0.2354329626
a_{10}	-0.9990632481

KKL model:

Koo and Kleinstreuer introduced a novel thermal conductivity that considers the random motion of nanoscale particles carrying a significant amount of fluid in their proximity. However, Brownian motion also contributes to thermal conductivity fluctuations. This includes a static component, k_{static}, and Brownian movement components, $k_{Brownian}$. The $k_{Brownian}$ component is explained using an approximation of Stokes flow and kinetic theory, aiding in estimating a fluid magnitude carried by nano-particles. Consequently, the model provides the thermal conductivity as follows:

$$k_{nf} = k_{static} + k_{Brownian},$$

Thus $\dfrac{k_{static}}{k_f} = 1 + \dfrac{3\left(\dfrac{k_s}{k_f} - 1\right)\varphi}{\left(\dfrac{k_s}{k_f} + 2\right) - \left(\dfrac{k_s}{k_f} - 1\right)\varphi}.$

The expression involves the nanoparticle volume fraction (φ) with subscripts indicating base fluid (f) and nanoparticles (s):

$$k_{Brownian} = 5 * 10^4 \beta\varphi\rho_f Cp_f \sqrt{\frac{k_b T}{\rho_s d_s}} f(T,\varphi,d_s)$$

The Boltzmann constant κ_b is defined as 1.3807×10^{-23} J/K and d_s represents the particle diameter. In the presence of particles with nano dimensions and base fluids, there exists an interfacial thermal resistance, also known as Kapitsa resistance. This resistance weakens the effective thermal conductivity. Li later revised this model by incorporating the f and β functions into a G function, which consolidates the effects arising from the particle diameter, volume fraction, and temperature. The nature of nanoparticles influences this G function. When considering the recommendation for Kapitsa resistance:

$$R_f + \frac{d_s}{k_s} = \frac{d_s}{k_{s,eff}}$$

The G function is established as:

$$G(T,\varphi,d_s) = \left(a_1 + a_2 \ln(d_s) + a_3 \ln(\varphi) + a_4 \ln(d_s) + a_5 \ln(d_s)^2\right)\ln(T) + \left(a_6 + a_7 \ln(d_s) + a_8 \ln(\varphi) + a_9 \ln(\varphi)\ln(d_s) + a_{10} ln(d_s)^2\right), \quad (13)$$

for $0.01 \le \varphi \le 0.04$, $300 < T < 325$, T in Kelvin.

Furthermore, coefficients a_i (for i = 1…10) for Al_2O_3-H_2O nano-liquids, with corresponding R^2 values of 96% and 98%, are provided in Table 2. Ultimately, Koo-Kleinstreuer-Li model is expressed as:

$$k_{Brownian} = 5 \times 10^4 \beta\varphi\rho_f Cp_f \sqrt{\frac{\kappa_b T}{\rho_s d_s}} G(T,\varphi,d_s)$$

Applying the same approach, the effective viscosity is determined as:

$$\mu_{nf} = \mu_{static} + \mu_{Brownian}$$

The expression for μ_{Static}, as proposed by Brinkman, is given by $\mu_{Static} = \mu_f / (1-\varphi)^{2.5}$. Additionally, the contribution of Brownian movement to viscosity $(\mu_{Brownian})$ is defined as $\mu_{Brownian} = (k_{Brownian} / k_f) \times (\mu_f / Pr)$. The following are the non-dimensional variables as mentioned below:

$$\begin{gathered} u = s\breve{a}f'(\eta), \;\; v = \frac{-R}{R+r}\sqrt{\breve{a}\nu_f}\, f(\eta), \;\; p = \rho s^2 \breve{a}^2 P(\eta) \\ T = T_\infty\left[1 + (\theta_w - 1) + \theta(\eta)\right], \;\; \eta = \sqrt{\frac{\breve{a}}{\nu_f}}\, r, \;\; \phi(\eta) = \frac{C - C_\infty}{C_w - C_\infty}. \end{gathered} \quad (14)$$

Utilizing the aforementioned transformations, the reduced equations with boundary constraints are as follows:

$$\epsilon_1 P' - \frac{1}{\kappa+\eta} f'^2 = 0, \tag{15}$$

$$\epsilon_1 \frac{2\kappa}{\kappa+\eta} P = \epsilon_1\epsilon_2\left(f''' + \frac{1}{\kappa+\eta} f'' - \frac{1}{(\kappa+\eta)^2} f'\right) + \frac{\kappa}{\kappa+\eta} ff'' - \frac{\kappa}{\kappa+\eta}(f')^2 + \frac{\kappa}{(\kappa+\eta)^2} ff' - \epsilon_1 \frac{2\beta}{(\eta+b)^4}\theta, \tag{16}$$

$$\begin{aligned}&\epsilon_3 \frac{k_{nf}}{k_f}\frac{1}{Pr}\left(\theta'' + \frac{1}{\kappa+\eta}\theta'\right) + \frac{\kappa}{\kappa+\eta} f\theta' + \epsilon_3 \frac{Rd}{Pr}\left(((\theta_w-1)\theta+1)^3\left(\theta'' + \frac{1}{\kappa+\eta}\theta'\right)\right) + 3\epsilon_3 \frac{Rd}{Pr}\left(((\theta_w-1)\theta+1)^2(\theta_w-1)\theta'^2\right)\\ &+ \frac{2\epsilon_3\beta\lambda(\theta-\epsilon)}{Pr}\frac{1}{(\eta+b)^3}\left(\frac{\kappa}{\kappa+\eta} f\left\{1 - \frac{2}{(\eta+b)^2}\right\} - \frac{f'}{\eta+b}\right) + \epsilon_2\epsilon_3 Ec\left(f'' + \frac{1}{\kappa+\eta} f'\right)^2 = 0,\end{aligned} \tag{17}$$

$$\phi'' + \frac{1}{\kappa+\eta}\phi' + \frac{\kappa}{\kappa+\eta} Sc\phi' f - Sc\delta\phi = 0. \tag{18}$$

The corresponding boundary conditions are:

$$\begin{aligned}&f = 0, f' = 1 + S_1\left(f''(0) - \frac{f'(0)}{k_f}\right) + S_2\left(f'''(0) + \frac{1}{k_f} f''(0) - \frac{1}{k_f^{\,2}} f'(0)\right),\\ &\frac{k_{nf}}{k_f}\theta' = Bi_t[\theta(0)-1], \quad \phi' = Bi_c[\phi(0)-1] \quad \text{at} \quad \eta = 0,\\ &f' \to 0, \quad f'' \to 0, \quad \theta \to 0, \quad \phi \to 0 \quad \text{as} \quad \eta \to \infty,\end{aligned} \tag{19}$$

where,

$$\epsilon_1 = \left[\frac{1}{(1-\varphi) + \varphi\frac{\rho_s}{\rho_f}}\right], \quad \epsilon_2 = \left[\frac{1}{(1-\varphi)^2} + \frac{k_{Brownian}}{Prk_f}\right], \quad \epsilon_3 = \left[\frac{1}{(1-\varphi) + \varphi\frac{(\rho Cp)_s}{(\rho Cp)_f}}\right].$$

Eliminating the pressure $P(\eta)$ from equation (15) and equation (16) yields:

$$\epsilon_1\epsilon_2\left(f'''' + \frac{2}{\kappa+\eta} f''' - \frac{1}{(\kappa+\eta)^2} f'' + \frac{1}{(\kappa+\eta)^3} f'\right) + \frac{\kappa}{\kappa+\eta}(ff''' - f''f') + \frac{\kappa}{(\kappa+\eta)^2}(ff'' - f'^2) - \frac{\kappa}{(\kappa+\eta)^3} ff' - \frac{2\epsilon_1\beta}{(\eta+b)^4}\left(\left(\frac{1}{\kappa+\eta} - \frac{4}{\eta+b}\right)\theta + \theta'\right) = 0, \tag{20}$$

where,

- $\kappa = \sqrt{\frac{\breve{a}}{\nu_f}}R$: (curvature parameter),
- $\theta_w = \frac{T_w}{T_\infty}$: (temperature difference parameter),
- $\beta = \frac{\gamma\mu_0 K_1 T_\infty(\theta_w - 1)\rho_f}{2\pi\mu_f^{\,2}}$: (ferrohydrodynamic interaction),
- $b = \sqrt{\frac{\breve{a}}{\nu_f}}g$: non-dimensional distance,
- $Pr = \frac{\nu_f(\rho Cp)_f}{k_f}$: Prandtl number,
- $Rd = \frac{16\sigma^* T_\infty^{\,3}}{3k_f k^*}$: radiation parameter,
- $\epsilon = \frac{1}{(1-\theta_w)}$: Curie temperature,
- $\lambda = \frac{\breve{a}\mu_f^{\,2}}{\rho_f T_\infty(\theta_w - 1)k_f}$: heat dissipation parameter,
- $Ec = \frac{(\breve{a}s)^2}{(Cp)_f T_\infty(\theta_w - 1)}$: Eckert number,
- $Sc = \frac{\nu_f}{D_m}$: Schmidt number,
- $\delta = \frac{k_r}{\breve{a}}$: non-dimensional chemical reaction,

- $S_1 = \lambda_1 \sqrt{\frac{\breve{a}}{\nu_f}}$: first order slip parameter,
- $S_2 = \lambda_1 \frac{\breve{a}}{\nu_f}$: second order slip parameter,
- $Bi_t = \frac{h_t}{k_f}\sqrt{\frac{\nu_f}{\breve{a}}}$: thermal Biot number,
- $Bi_c = \frac{k_c}{D_m}\sqrt{\frac{\nu_f}{\breve{a}}}$: solutal Biot number.

3. Entropy Generation

To ensure efficiency of the system, calculation of entropy generated by the heat transport and the flow is essential. Consequently, entropy is determined [31]:

$$Sg = \frac{k_{nf}}{T_\infty{}^2}\left(1 + \frac{16\sigma^* T^3}{k_f k^*}\right)\left(\frac{\partial T}{\partial r}\right)^2 + \frac{\mu_{nf}}{T_\infty}\left(\frac{\partial u}{\partial r} + \frac{u}{R+r}\right)^2, \tag{21}$$

The dimensionless form is in accordance with the given conditions:

$$Ng = \frac{k_{nf}}{k_f}\alpha_1\theta'^2\left[1 + Rd\left(\theta(\theta_w - 1) + 1\right)^3\right] + \epsilon_2 Ec\Pr\left(f'' + \frac{f'}{\kappa+\eta}\right)^2. \tag{22}$$

The equation for determining Be is as follows:

$$Be = \frac{\text{entropy generation owing to thermal transfer}}{\text{total entropy generation}}$$

$$Be = \frac{\frac{k_{nf}}{k_f}\alpha_1\theta'^2\left[1 + Rd(1 + \theta(\theta_w - 1))^3\right]}{\frac{k_{nf}}{k_f}\theta'^2\alpha_1\left[1 + Rd\left(\theta(\theta_w - 1) + 1\right)^3\right] + \epsilon_2 Br\left(f'' + \frac{f'}{\kappa+\eta}\right)^2}. \tag{23}$$

where $\alpha_1 = (T_w - T_\infty)/T_\infty$ is the temperature ratio parameter.

4. Results and Discussions

This section presents significant findings obtained from solving a boundary value problem outlined in equations (15)-(20). The primary objective of the investigation using KKL model is to examine the operative thermal conductivity as well as viscosity characteristics of nano-liquid in a curved surface with a magnetic dipole, radiative (nonlinear) heat flux, chemical reaction, and viscous dissipation. Graphical representations of velocity, thermal, and concentration gradients are afforded. By applying similarities, the governing PDE are converted into ODE. The equations are addressed using the RKF-4th-5th approach with shooting scheme. Graphical analysis is conducted for various parameters affecting velocity, temperature as well as concentration. Additionally, this study explores graphical results for entropy and the Bejan number. The thermophysical belongings of carrier liquids and nano-particles are detailed in Table 1 using default numerical values: $\kappa = 3.5,\ \beta = 1.1,\ b = 1,\ \theta_w = 1.5,\ Rd = 2,\ Sc = 2,\ \delta = 1,\ S_1 = 0.2,\ S_2 = 0.2,\ Bi_t = 0.5,\ Bi_c = 0.5,\ Pr = 6.2,\ \epsilon = 0.5,\ \lambda = 0.5,\ Ec = 0.01$.

4.1. Velocity Profile

Figure 2 shows that influence of κ on velocity field. The figure indicates that rise in κ guides to an enhancement in fluid velocity. Specifically, an upward trend in κ corresponds to a larger radius, causing the liquid to move more swiftly across the sheet. Consequently, the rise in κ leads to a reduction in fluid viscosity, thereby causing an automatic elevation in the velocity gradient. Figure 3 demonstrates that $f'(\eta)$ rises on enhancing ferrohydrodynamic parameter. This occurs due to intensified movement and alignment of magnetic particles within the ferrofluid, leading to an enhanced interaction with the magnetic field. In the later stages, as β increases, the resistance force, called as Lorentz strength increases, reducing velocity of fluid particles are away from surface. In Fig. 4, velocity reduces with a rise in magnetic dipole dimensionless distance. This phenomenon is attributed to a larger dimensionless distance, represented by b, resulting in an escalation of Lorentz force resistance. Consequently, this increased resistance causes reduction in velocity near the boundary. Figure 5 clearly depicts how the decrease in the velocity slip factor influences the velocity distribution. In stretching surface as well as flow of fluid, an augmentation in S_1 induces heterogeneous velocity, leading to reduction in the overall velocity distribution. The velocity profile increases with an enhances in second-order slip (S_2) in Fig. 6, because an enhanced slip at the fluid-solid interface promotes greater fluid movement, leading to an overall rise in the velocity profile.

4.2. Temperature Profile

The investigation into the effect of κ on $\theta(\eta)$ is elucidated in Fig. 7. It is noteworthy that κ is inversely proportional to kinematic viscosity by definition. Consequently, an increase in κ corresponds to a reduction in the $\theta(\eta)$ of the fluid. When ferrohydrodynamic interaction rises, the temperature profile declines in Fig. 8, because the interaction enhances the heat transfer process. Increased ferrohydrodynamic effects often lead to greater fluid velocity and more efficient thermal conduction, which can reduce the temperature gradient near the sheet. This results in a lower overall temperature profile.

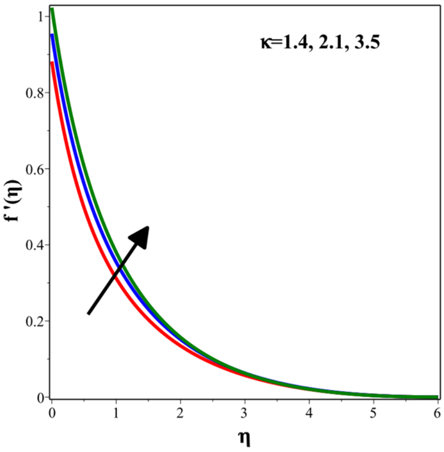

Fig. 2. Variation of $f'(\eta)$ for κ values.

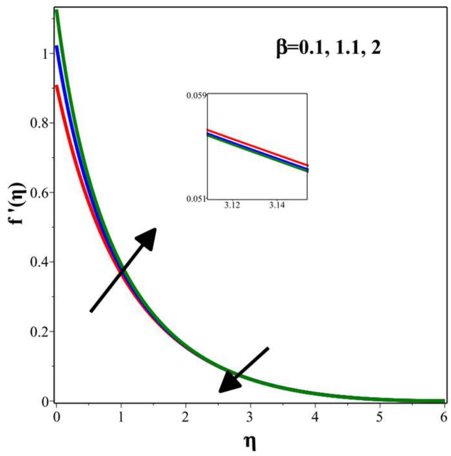

Fig. 3. Variation of $f'(\eta)$ for β values.

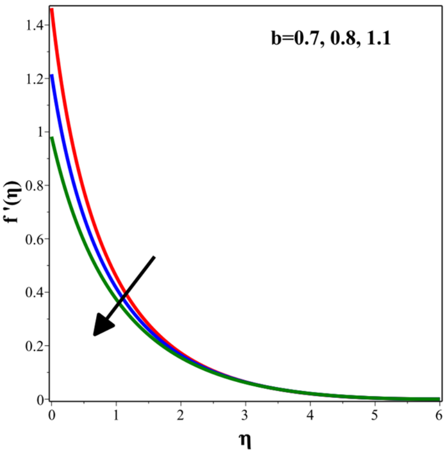

Fig. 4. Variation of $f'(\eta)$ for b values.

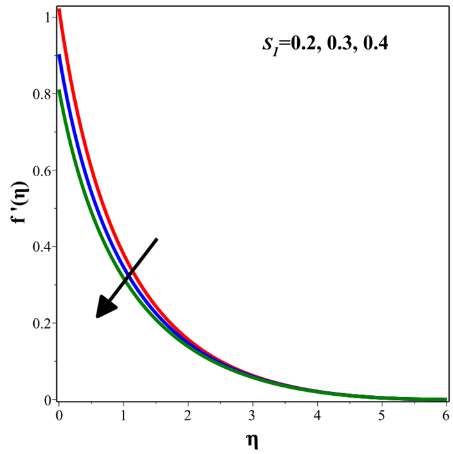

Fig. 5. Variation of $f'(\eta)$ for S_1 values.

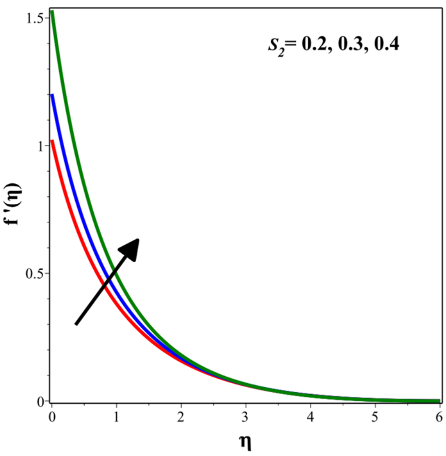

Fig. 6. Variation of $f'(\eta)$ for S_2 values.

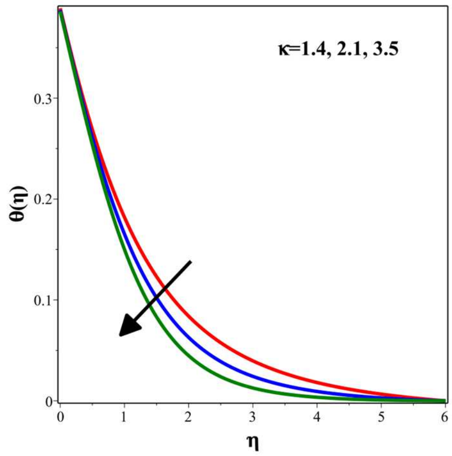

Fig. 7. Variation of $\theta(\eta)$ for κ values.

Figure 9 shows that, the temperature profile increases near the boundary due to stretching effects. However, as the heat dissipation term increases, heat is removed from the system, causing the temperature to decrease away from the boundary. The temperature profile increases initially, and at a later stage near the boundary, it reduces with an enhances in the Curie temperature (ϵ) as in Fig. 10. This is because, initially, the elevated Curie temperature promotes higher overall temperatures, but as it increases further, localized cooling near the boundary becomes more dominant, leading to subsequent reduce in temperature. In Fig. 11, temperature profile exhibits a decrease with an escalating Prandtl number (Pr). This phenomenon is attributed to the diminished thermal diffusivity, resulting in a slower heat transfer rate and, consequently, lower temperatures. In Fig. 12, the temperature profile demonstrates an increase with an elevated temperature difference parameter (θ_w). This is Assigned to the intensified radiative heat transfer, leading to greater temperatures across the system. In Fig. 13, the temperature profile exhibits an increase with an elevated radiation parameter (Rd). This is attributed to the heightened radiative heat transfer, resulting in higher temperatures within the system.

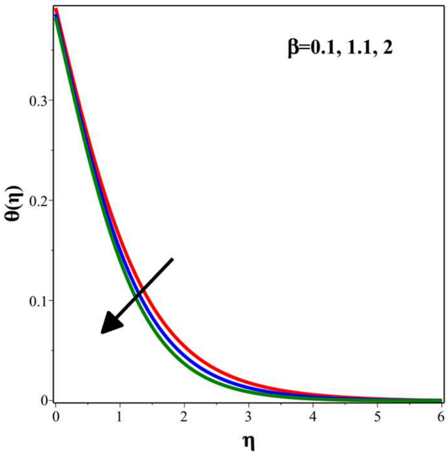

Fig. 8. Variation of $\theta(\eta)$ for β values.

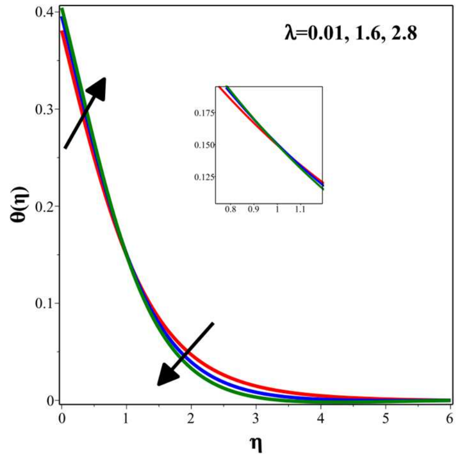

Fig. 9. Variation of $\theta(\eta)$ for λ values.

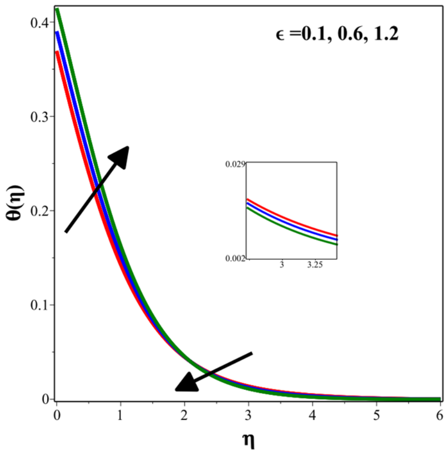

Fig. 10. Variation of $\theta(\eta)$ for ϵ values.

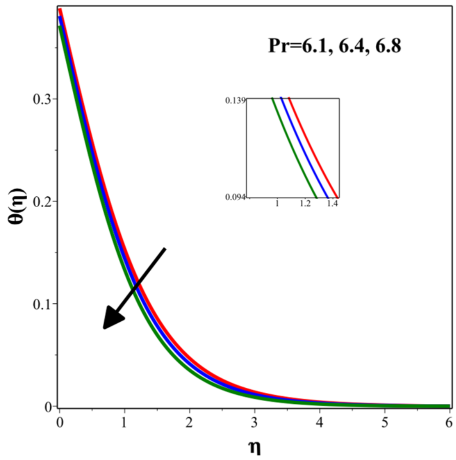

Fig. 11. Variation of $\theta(\eta)$ for Pr values.

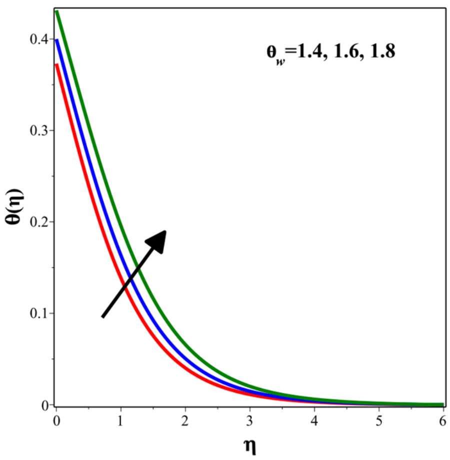

Fig. 12. Variation of $\theta(\eta)$ for θ_w values.

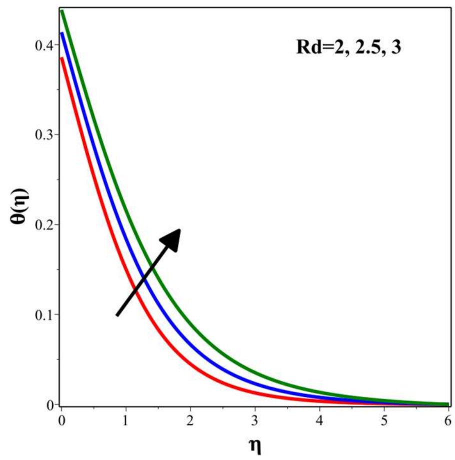

Fig. 13. Variation of $\theta(\eta)$ for Rd values.

In Fig. 14, the effect of Eckert number on the $\theta(\eta)$ is illustrated. A rise in Ec corresponds to an enhancement in the $\theta(\eta)$, as Ec represents the ratio between kinetic energy to enthalpy. With greater values of Ec, there is a rise in kinetic energy, leading to an elevated temperature profile. The temperature profile graph depicted in Fig. 15, illustrates the impact of elevated thermal Biot numbers (Bi_t). As the Biot number increases, there is a noticeable enhancement in heat transfer through convection. However, a prominent escalation in the temperature field is observed.

4.3. Concentration Profile

In Fig. 16, the concentration rises conjunction with an increasing curvature parameter (κ), due to the heightened stretching effect caused by greater curvature. This increased curvature results in more significant fluid deformation and enhanced mass transfer. Consequently, there is a thicker concentration boundary layer, leading to an overall concentration increase near the curved region.

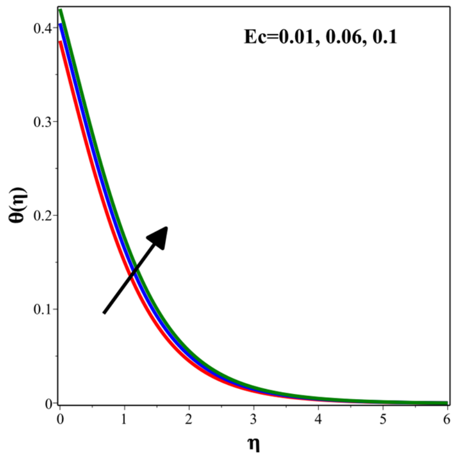

Fig. 14. Variation of $\theta(\eta)$ for Ec values.

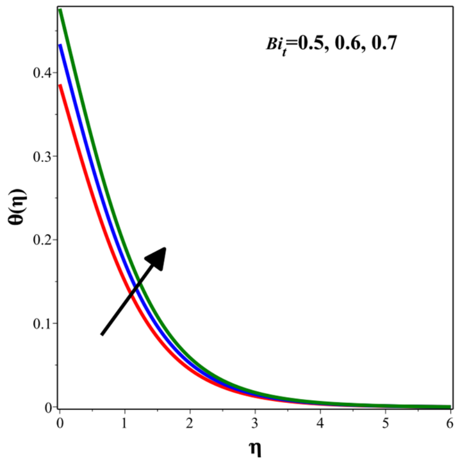

Fig. 15. Variation of $\theta(\eta)$ for Bi_t values.

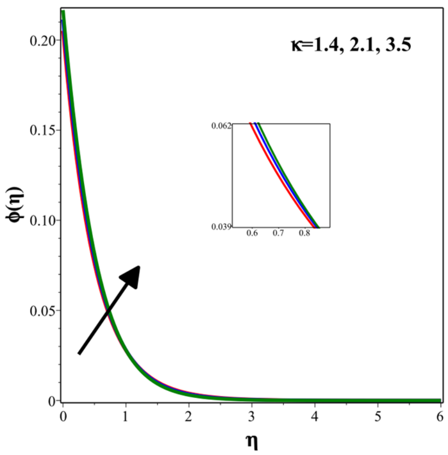

Fig. 16. Variation of $\phi(\eta)$ for κ values.

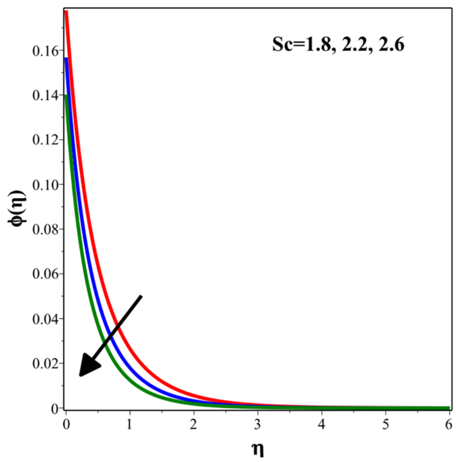

Fig. 17. Variation of $\phi(\eta)$ for Sc values.

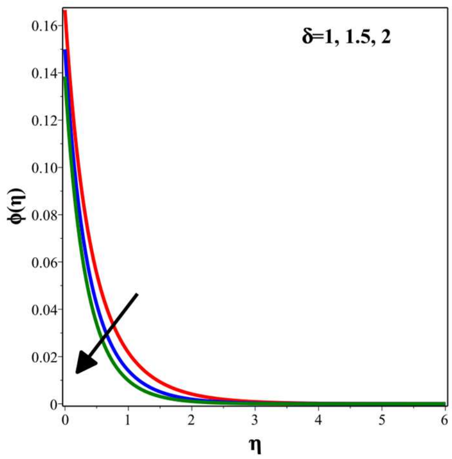

Fig. 18. Variation of $\phi(\eta)$ for δ values.

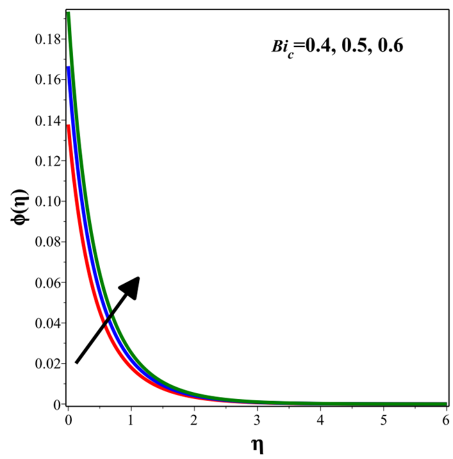

Fig. 19. Variation of $\phi(\eta)$ for Bi_c values.

In Fig. 17, the concentration profile decreases as the Schmidt number increases. This occurs because the Schmidt number is inversely related to mass diffusivity. As a result, higher values of the Schmidt number lead to reduced mass diffusion, which in turn decreases the concentration profile. In Fig. 18, the concentration profile declines with an increasing chemical reaction parameter (δ) due to the accelerated reaction rate, resulting in the rapid consumption or conversion of the involved species (fluid chemical). This leads to a decrease in its concentration near the curved region. In Fig. 19, the concentration profile exhibits an increase with an escalating concentration Biot number (Bi_c), indicating more pronounced convective transport compared to diffusion. This dominance of convective transport facilitates greater mass transfer. However, overall concentration increases near the curved region.

4.4. Entropy Generation

In the presence of large Br, thermal transfer through conduction is dominated by viscous heating, leading to an elevation in fluid temperature. The increase in temperature induces heightened movement of charged particles within the fluid, driven by thermal radiation, resulting in a temperature rise with a higher radiation parameter (Rd).

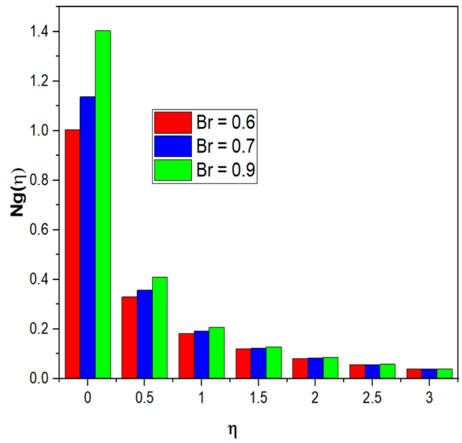

Fig. 20. Variation of $Ng(\eta)$ for Br values.

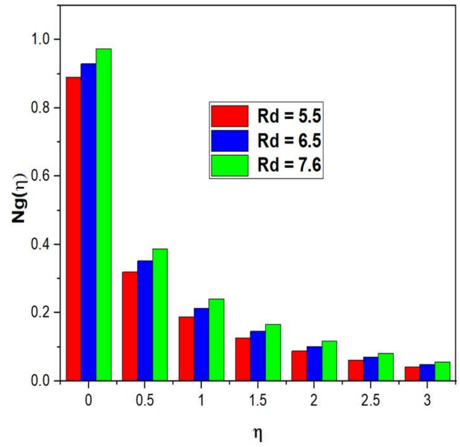

Fig. 21. Variation of $Ng(\eta)$ for Rd values.

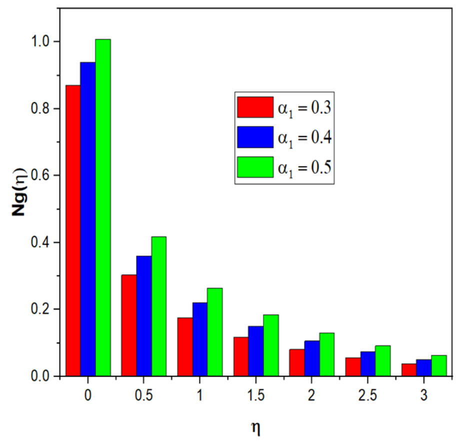

Fig. 22. Variation of $Ng(\eta)$ for α_1 values.

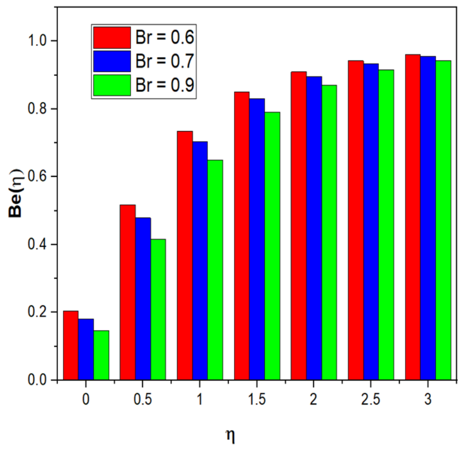

Fig. 23. Variation of $Be(\eta)$ for Br values.

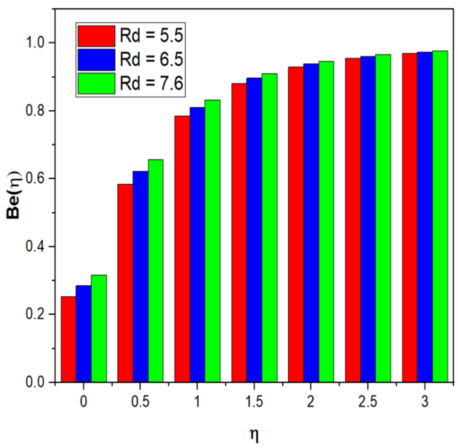

Fig. 24. Variation of $Be(\eta)$ for Rd values.

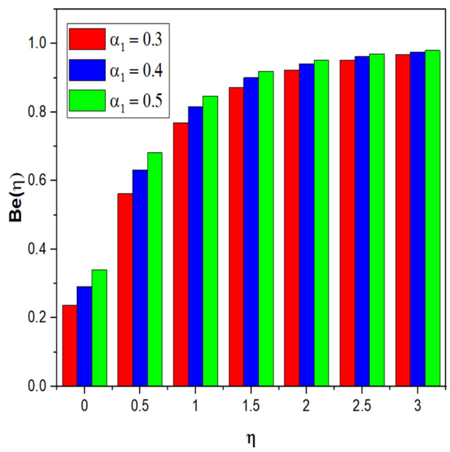

Fig. 25. Variation of $Be(\eta)$ for α_1 values.

As the temperature increases, it triggers additional phenomena like internal displacement as well as vibrations, contributing to an augmentation in fluid entropy. Entropy generation further increases with an elevated temperature ratio parameter (α_1), as a higher temperature ratio indicates larger temperature gradients, amplifying heat transfer and consequently raising energy dissipation and entropy production. Therefore, an increase in Br, Rd, and α_1 result in an elevation of entropy generation $(Ng(\eta))$ in the fluid, as depicted in Figs. 20, 21 and 22. The Br significantly influences the Be, as depicted in Fig. 23. As Br improves, there is a reduction in the Bejan number. This decline occurs when viscous irreversibility begins to dominate over heat transfer irreversibility. Figure 24 illustrates how Rd affects the Be. With a rise in radiation emission, there is a corresponding increase in the disorderliness within the closed system, leading to a rise in the radiative constant. Consequently, the Bejan number of the system also increases. In Fig. 25, as the temperature ratio parameter increases, the Bejan number increases because higher temperature ratios correspond to greater thermal gradients, which enhance irreversibility and entropy generation, thereby elevating the Bejan number.

Table 3. Parameters and their values.

Parameter	Coded Symbol	Level		
		-1 (Low)	0 (Medium)	1 (High)
Ec	A	0.01	0.03	0.05
Pr	B	6	6.2	6.4
Rd	C	2	2.2	2.4

Table 4. Experimental design.

Runs	Coded Values			Real Values			Response *Ng*
	A	B	C	*Ec*	*Pr*	*Rd*	
1	-1	-1	-1	0.01	6	2	0.391159
2	1	-1	-1	0.05	6	2	0.396802
3	-1	1	-1	0.01	6.4	2	0.386175
4	1	1	-1	0.05	6.4	2	0.391935
5	-1	-1	1	0.01	6	2.4	0.419545
6	1	-1	1	0.05	6	2.4	0.424557
7	-1	1	1	0.01	6.4	2.4	0.414751
8	1	1	1	0.05	6.4	2.4	0.419905
9	-1	0	0	0.01	6.2	2.2	0.403272
10	1	0	0	0.05	6.2	2.2	0.408675
11	0	-1	0	0.03	6	2.2	0.408433
12	0	1	0	0.03	6.4	2.2	0.403572
13	0	0	-1	0.03	6.2	2	0.391460
14	0	0	1	0.03	6.2	2.4	0.419649
15	0	0	0	0.03	6.2	2.2	0.405963
16	0	0	0	0.03	6.2	2.2	0.405963
17	0	0	0	0.03	6.2	2.2	0.405963
18	0	0	0	0.03	6.2	2.2	0.405963
19	0	0	0	0.03	6.2	2.2	0.405963
20	0	0	0	0.03	6.2	2.2	0.405963

Table 5. ANOVA table.

Source	Degree of freedom	Adj. Sum of Squares	Adj. Mean squares	F-Value	P-Value
Model	9	0.0021	0.0002	2896357.1600	0.0000
Linear	3	0.0021	0.0007	8685187.8900	0.0000
Ec	1	0.0001	0.0001	895900.2800	0.0000
Pr	1	0.0001	0.0001	718734.7200	0.0000
Rd	1	0.0020	0.0020	24440928.6800	0.0000
Square	3	0.0000	0.0000	2980.2900	0.0000
Ec Ec*	1	0.0000	0.0000	3.4800	0.0920
Pr Pr*	1	0.0000	0.0000	51.2900	0.0000
Rd Rd*	1	0.0000	0.0000	5661.8100	0.0000
2-Way Interaction	3	0.0000	0.0000	903.3100	0.0000
*Ec*Pr*	1	0.0000	0.0000	103.9700	0.0000
*Ec*Rd*	1	0.0000	0.0000	2355.0600	0.0000
*Pr*Rd*	1	0.0000	0.0000	250.9000	0.0000
Error	10	0.0000	0.0000		
Lack-of-Fit	5	0.0000	0.0000	*	*
Pure Error	5	0.0000	0.0000		
Total	19	0.0021			

5. Statistical Analysis: Response Surface Methodology

Statistical analysis of entropy generation is investigated using (Ec) Eckert number, (Rd) radiation parameter, and (Pr) Prandtl number within specific intervals $(0.01 \le Ec \le 0.05, 6 \le Pr \le 6.4,$ and $0.1 \le Rd \le 0.5)$. Table 3 shows these parameters and their respective ranges. RSM is utilized to comprehend how these parameters affect the dependent variable, conceptualized as a surface. An experimental design is formulated using a face-centered central composite design, as described in Table 4, which encompasses three variables across 20 experimental trials. The standard quadratic model integrates linear, interaction, and quadratic terms for each parameter to capture the intricacies of the relationship:

$$Nu = a_1 Ec + a_2 Pr + a_3 Rd + a_4 EcPr + a_5 EcRd + a_6 PrRd + a_7 Ec^2 + a_8 Pr^2 + a_9 Rd^2 + a_{10} \quad (24)$$

In the RSM paradigm, the suggested coefficients are denoted as $a_i (i = 1, \ldots, 10)$. This model facilitates the analysis of how Ec, Pr, and Rd impact a responding variable (Ng). The ANOVA table in Table 5 divides variation into multiple sources and differences among groups by comparing the means of each group. For a parameter to be statistically significant, its p-value must be below 0.05, which corresponds to a 95% significance level. The analysis shows that the quadratic term of the variable does not significantly influence the response variable. Furthermore, the experimental design reports a high coefficient of determination (R^2) of 99.99%, indicating a strong model fit. Various residual plots for Ng, shown in Fig. 26, help evaluate the model's accuracy. The normal probability plot suggests a linear relationship, and the accompanying histogram displays a bell-shaped distribution, indicative of standard statistical behavior of the parameters. In addition, the residual errors are recorded as 0.00001, demonstrating the model accuracy and fit. Figure 27 shows the Pareto chart of Ec, Pr, as well as Rd in linear, interactive, and quadratic forms. It illustrates that over the critical point, which is at 2, all parameters are deemed significant factors for the system. Notably, the Eckert number (Ec) emerges as the most influential parameter, suggesting that manipulating Ec holds more significance in affecting outcomes compared to adjustments in Pr and Rd.

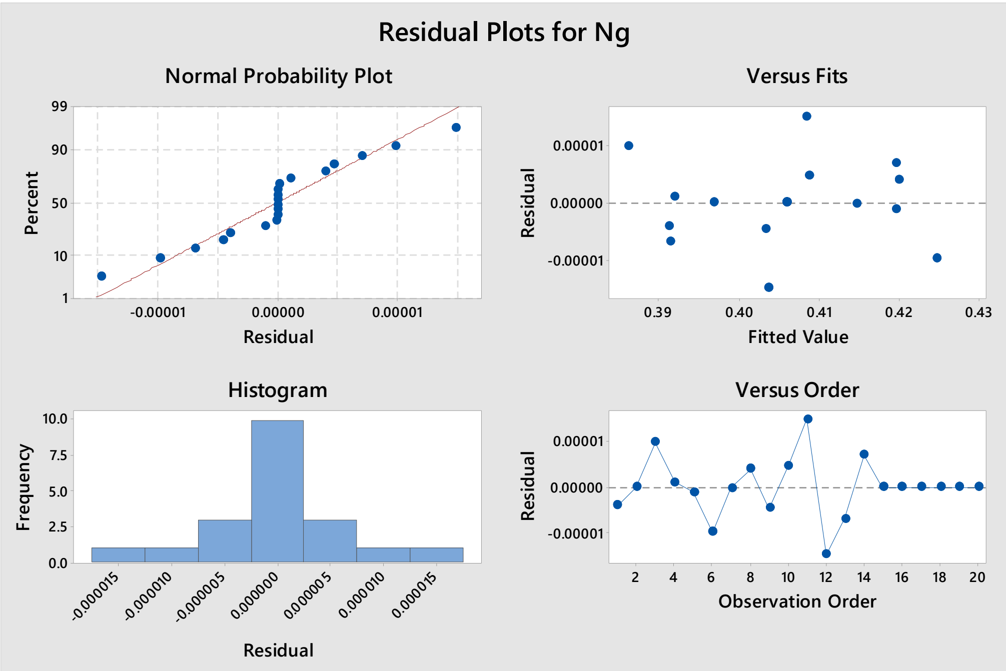

Fig. 26. Standardized Residual plots for Ng.

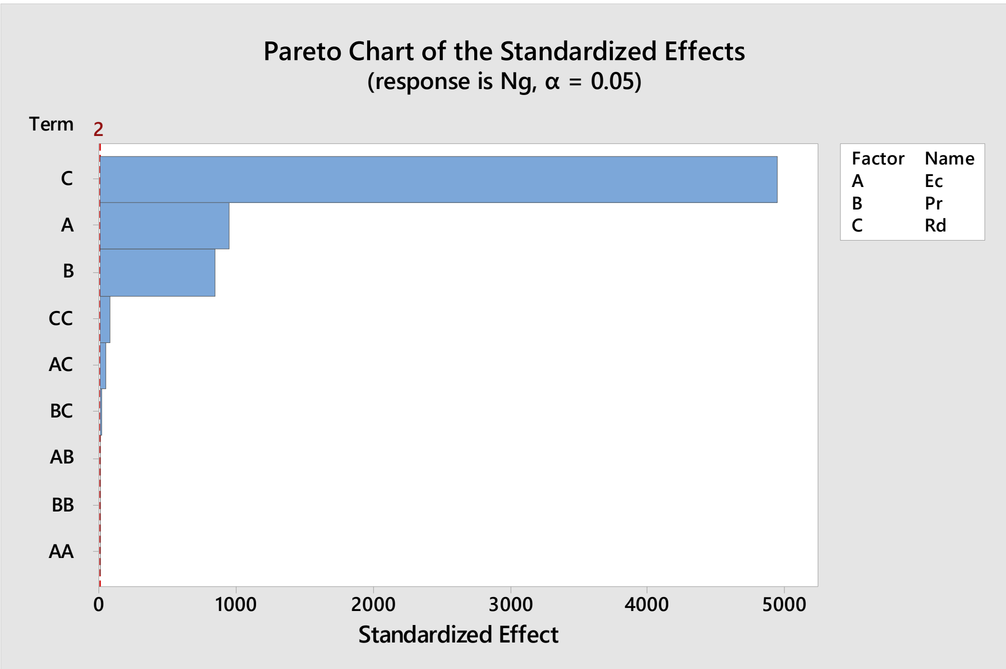

Fig. 27. Pareto chart of standardized effects.

5.1. Statistical Elucidation

The statistical model for assessing entropy generation is:

$$\begin{aligned} Ng = {} & 0.32596+0.16802\,Ec-0.02716\,Pr+0.108751\,Rd+0.0253\,Ec*Ec+0.000973\,Pr*Pr \\ & -0.010222\,Rd*Rd+0.008121\,Ec*Pr-0.038652\,Ec*Rd+0.001262\,Pr*Rd \end{aligned} \tag{25}$$

From above equation, the linear term coefficients suggest that Eckert number and radiation parameter have positive impact on entropy generation and the Prandtl number has negative impact on response variable. Figure 28 illustrates interaction between two of the three factors while holding the third constant. Notably, when the Eckert number is at its peak and the radiation parameter is elevated, the surface plot depicting the relationship between Eckert number and radiation parameter reveals the maximum entropy generation. Furthermore, it is noticed that *Pr* and *Rd* is high, entropy generated within the system reaches its highest levels.

5.2. Sensitivity analysis

The parameters are coded as $A-Ec$, $B-Pr$ and $C-Rd$ to determine sensitivity of response variable:

$$\begin{aligned} Ng = {} & 0.32596+0.16802\,{*A}-0.02716\,{*B}+0.108751\,{*C}+0.000973\,{*B^2}-0.010222\,{*C^2} \\ & +0.008121\,{*A*B}-0.038652\,{*A*C}+0.001262\,{*B*C} \end{aligned} \tag{26}$$

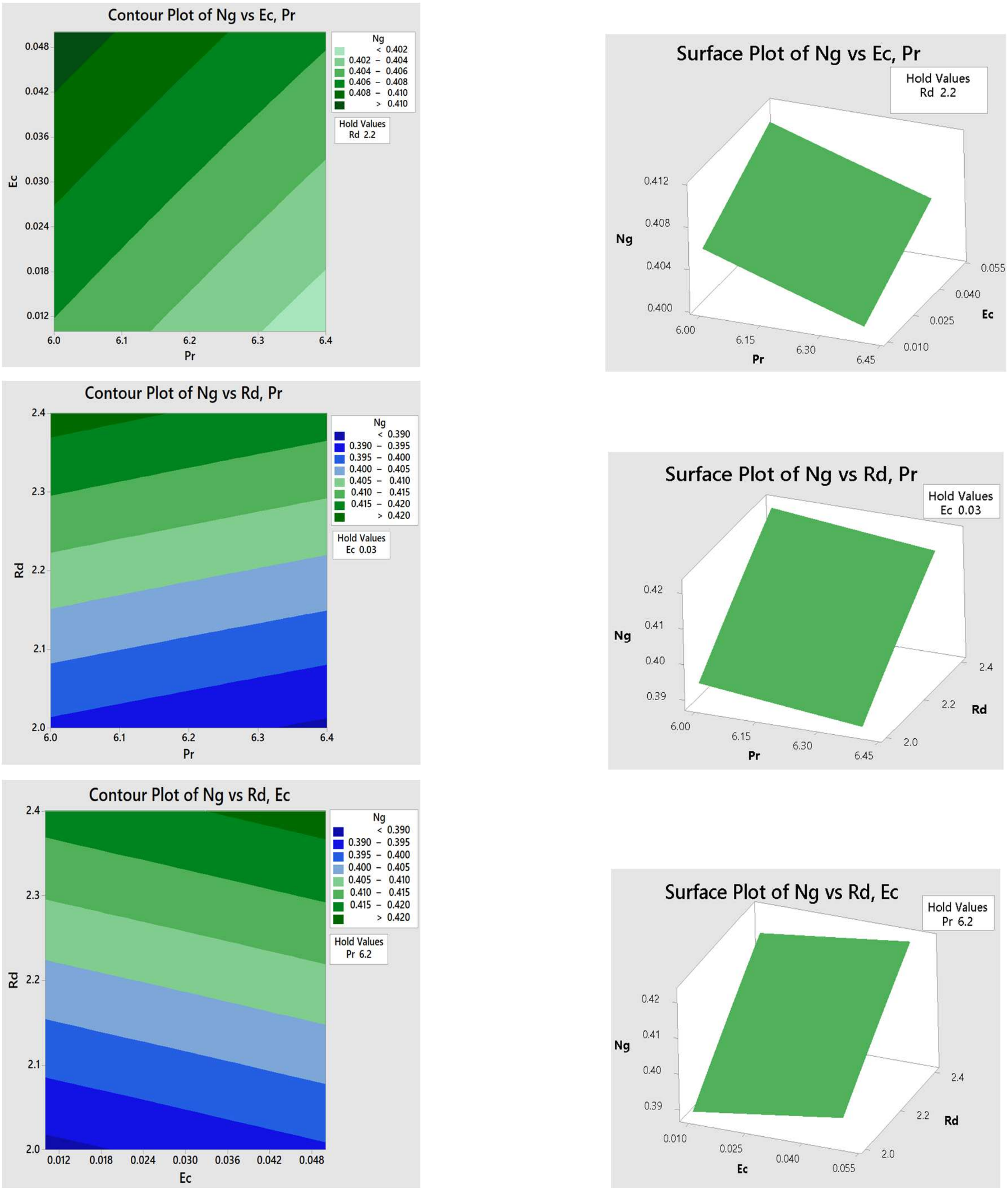

Fig. 28. Contour and 3D surfaces for *Ng*.

Table 6. Sensitivity of Ng for the medium level of A.

B	C	Sensitivity $\frac{\partial Ng}{\partial A}$	$\frac{\partial Ng}{\partial B}$	$\frac{\partial Ng}{\partial C}$
	-1	0.198551	-0.03037	0.127933
-1	0	0.159899	-0.02911	0.107489
	1	0.121247	-0.02784	0.087045
	-1	0.206672	-0.02842	0.129195
0	0	0.16802	-0.02716	0.108751
	1	0.129368	-0.0259	0.088307
	-1	0.214793	-0.02648	0.130457
1	0	0.176141	-0.02521	0.110013
	1	0.137489	-0.02395	0.089569

By applying partial differentiation to the specified model, the sensitivity functions can be established. This approach involves determining the response of the model to changes in its parameters:

$$\begin{aligned}\frac{\partial Ng}{\partial A} &= 0.16802 + 0.008121B - 0.038652C \\ \frac{\partial Ng}{\partial B} &= -0.02716 + 2 * 0.000973B + 0.008121A + 0.001262C \\ \frac{\partial Ng}{\partial C} &= 0.108751 - 2 * 0.010222C - 0.038652A + 0.001262B\end{aligned} \tag{27}$$

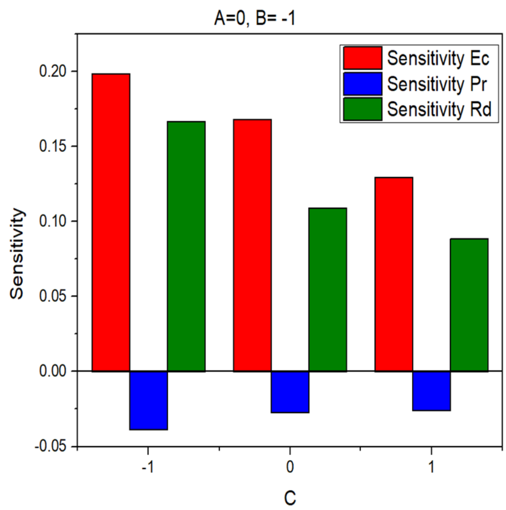

Fig. 29. Sensitivity at low level of B.

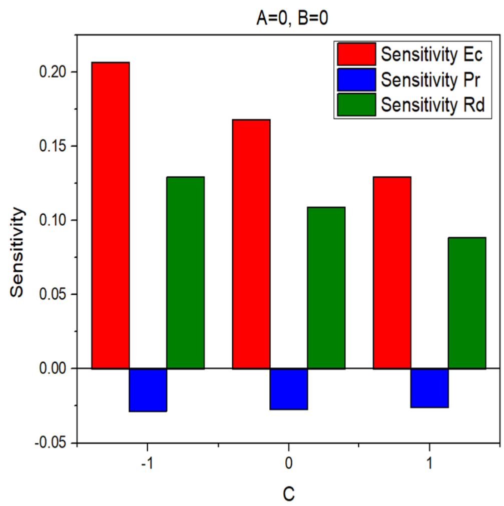

Fig. 30. Sensitivity at medium level of B.

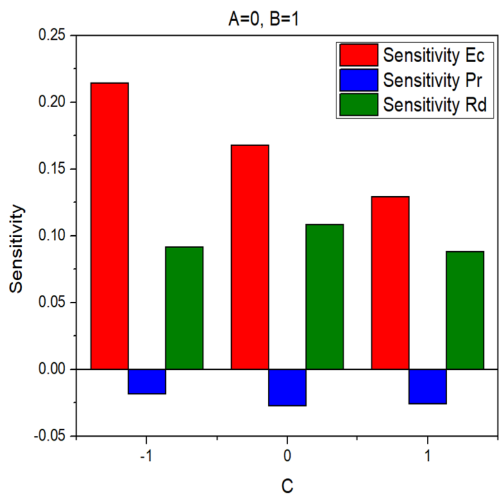

Fig. 31. Sensitivity at high level of B.

When variable A is set to a middle level, the sensitivity of the resulting variable is assessed for different values of variables B and C. Sensitivity is considered high if increasing a variable lead to an increase in entropy production, and low if it results in a decrease. The magnitude of this sensitivity highlights the importance of the variables under study. Figures 29 to 31 use bar graphs to visually and quantitatively illustrate the sensitivity across three distinct categories. Figure 29 shows positive sensitivity to Rd and Ec, while Pr exhibits negative sensitivity across all levels of C. This trend is consistent with the observations in Figs. 30 and 31. Specifically, Ec decreases consistently across all levels of C, while Pr decreases at low and medium levels of B, then increases from low to medium levels of C, and slightly increases at high levels of B. In contrast, Rd decreases as C levels increase from low to high at both low and medium levels of B. However, at high levels of B, Rd shows an increasing trend at low and medium levels of C, while a decreasing trend is observed at high levels of C. The system expected to experience its maximum entropy generation when $Ec = 0.05$, $Pr = 6$, and $Rd = 2.4$. Conversely, the system's minimal entropy occurs when $Ec = 0.01$, $Pr = 6.4$, and $Rd = 2$.

6. Concluding Review

In this research, we explored a 2D model describing the nano-fluid flow involving mass also thermic transfer of Al_2O_3 nano-particles over elongated curved sheet. The model incorporated a chemical reaction, magnetic dipole, radiative heat flux (non-linear), slip, and convective boundary constraints. The thermal as well as mass transfer processes were analyzed using the KKL model, and governing equations were numerically solved using RKF-4th-5th approach with a shooting scheme. The study presented velocity, thermal, and concentration profiles for specific flow conditions, highlighting the key features of this investigation as follows:

- The velocity profile shows an increase with higher values of κ and S_2, but a decrease with increasing b and S_1. However, in the context of ferrohydrodynamic interaction, the velocity profile exhibits an initial increase near the boundary followed by a decrease in the later stage.
- For the temperature profile, an augmentation is spotted in higher values of Ec, Rd, θ_w, and Bi_c, while a decrease is associated with lower values of κ, β, and Pr. On the other hand, with λ and ϵ, the temperature profile increases near the boundary and decreases in the later stage as λ and ϵ values increase.
- The concentration profile experiences a decrease with higher δ and Sc values, whereas it increases with a cumulative value of Bi_c and κ.
- Entropy generation is rises with higher values of Br, Rd, and α_1. However, when Be enhances with increasing Rd and α_1, it reduces with higher values of Br.
- At the point 2, all parameters become crucial to the system.
- At all B levels, Ec and Rd have a positive influence on sensitivity, but Pr has a negative impact.

The nanofluid flow in presence of magnetic dipole effects has numerous applications in biomedical and engineering sectors. Further studies on nanofluid can be carried out for bio-magnetic fluids. The researchers can extend this research work by considering different aspects of the flow. One can easily use the other similar statistical techniques to identify the optimized flow like RSM.

Author Contributions

F. Almeida conducted the numerical methodology and data analysis; K.G. Vidhya wrote the formal draft, P. Kumar played a role in conceptualization and methodology, B. Nagaraja conducted the formal analysis and final review. The manuscript was written through the contribution of all authors. All authors discussed the results, reviewed, and approved the final version of the manuscript.

Acknowledgments

Not applicable.

Conflict of Interest

The authors declared no potential conflicts of interest concerning the research, authorship, and publication of this article.

Funding

The authors received no financial support for the research, authorship, and publication of this article.

Data Availability Statements

The datasets generated and/or analyzed during the current study are available from the corresponding author on reasonable request.

Nomenclature

$\breve{a}$	Stretching constant [m]	Sc	Schmidt number
b	Non-dimensional distance	S_1	First order slip parameter
Bi_t	Thermal Biot number	S_2	Second order slip parameter
Bi_c	Solutal Biot number	T	Fluid temperature [K]
C	Fluid concentration [molm^{-3}]	T_w	Fluid temperature at the surface [K]
C_w	Fluid concentration at the surface [molm^{-3}]	T_∞	Ambient fluid temperature [K]
C_∞	Ambient fluid concentration [molm^{-3}]	u	Velocity compounds along s-direction [ms^{-1}]
Cp	Specific heat capacity [Jkg^{-1}K^{-1}]	u_w	Stretching constant [ms^{-1}]
D_m	Diffusion coefficient [m^{2}s^{-1}]	v	Velocity compounds along r-direction [ms^{-1}]

d_s	Particle diameter
Ec	Eckert number
g	Distance across the dipole
h_t	Convective heat transfers co-efficient [$Wm^{-2}K^{-1}$]
H	Magnetic field
k	Thermal conductivity [$Wm^{-1}K^{-1}$]
k_r	Chemical reaction rate
k_c	Convective mass transfer coefficient [$Wm^{-1}K^{-1}$]
k^*	Mean absorption coefficient
k_b	Boltzmann constant [J/K]
K_1	Ferromagnetic co-efficient
M	Magnetization
Pr	Prandtl number
p	Pressure [$kgm^{-1}s^{-2}$]
P	Dimensionless pressure
q_r	Radiation heat flux
r,s	Local coordinates
R	Radius of curvature
Rd	Radiation parameter

Greek letters

η	Dimensionless Space coordinate
κ	Dimensionless curvature parameter
ρ	Density of the fluid [kg/m^3]
ϕ	Dimensionless concentration
δ	Dimensionless chemical reaction
ν	Kinematic viscosity [M^2s^{-1}]
μ_0	Magnetic permeability
μ	Dynamic viscosity [$kgm^{-1}s^{-1}$]
λ_1	First order slip
λ_2	Second order slip
σ^*	Stefan Boltzmann constant
γ	Magnetic field strength on the source
β	Ferrohydrodynamic interaction
λ	Heat dissipation parameter
θ_w	Temperature difference parameter
ϵ	Curie temperature
θ	Dimensionless temperature

References

[1] Choi, S.U.S., Eastman, J.A., *Enhancing thermal conductivity of fluids with nanoparticles*, Argonne National Lab (ANL), Argonne, IL United States, No. ANL/MSD/CP-84938, CONF-951135-29, 1995.

[2] Hayat, T., Rashid, M., Alsaedi, A., MHD convective flow of magnetite-Fe3O4 nanoparticles by curved stretching sheet, *Results in Physics*, 7, 2017, 3107-3115.

[3] Sharma, R., Bisht, A., Numerical study of MHD flow and heat transfer of nanofluid along a nonlinear curved stretching surface, *AIP Conference Proceedings*, 1975(1), 2018, 030025.

[4] Usama, S., Nadeem, Khan, A.U., Stability analysis of Cu-H2O nanofluid over a curved stretching–shrinking sheet: existence of dual solutions, *Canadian Journal of Physics*, 97(8), 2019, 911-922.

[5] Jammalamadaka, S.R., Qiu, J., Ning, N., Predicting a stock portfolio with the multivariate Bayesian structural time series model: Do news or emotions matter?, *International Journal of Artificial Intelligence*, 17(2), 2019, 81-104.

[6] Sene, N., Second-grade fluid model with Caputo–Liouville generalized fractional derivative, *Chaos, Solitons & Fractals*, 133, 2020, 109631.

[7] Precup, R.E., Teban, T.A., Albu, A., Borlea, A.B., Zamfirache, I.A., Petriu, E.M., Evolving fuzzy models for prosthetic hand myoelectric-based control, *IEEE Transactions on Instrumentation and Measurement*, 69(7), 2020, 4625-4636.

[8] Koo, J., Kleinstreuer, C., Laminar nanofluid flow in micro heat-sinks, *International Journal of Heat and Mass Transfer*, 48(13), 2005, 2652-2661.

[9] Jie, J., Kleinstreuer, C., Thermal performance of nanofluid flow in microchannels, *International Journal of Heat and Fluid Flow*, 29(4), 2008, 1221-1232.

[10] Kandelousi, M.S., Sheikholeslami. M., KKL correlation for simulation of nanofluid flow and heat transfer in a permeable channel, *Physics Letters A*, 378(45), 2014, 3331-3339.

[11] Sheikholeslami, M., Ganji, D.D., Effect of adding nanoparticle on squeezing flow and heat transfer improvement using KKL model, *International Journal of Numerical Methods for Heat & Fluid Flow*, 27(7), 2017, 1535-1553.

[12] Mohammadein, S.A., Raslan, K., Abdel-Wahed, M.S., Abedel-Aal. E.M., KKL-model of MHD CuO-nanofluid flow over a stagnation point stretching sheet with nonlinear thermal radiation and suction/injection, *Results in Physics*, 10, 2018, 194-199.

[13] Kumar, R.N., Alam, R.J.G.M., Ahmad, I., Mahrous, Y.M., Gorji, M.R., Prasannakumara, B.C., Inspection of convective heat transfer and KKL correlation for simulation of nanofluid flow over a curved stretching sheet, *International Communications in Heat and Mass Transfer*, 126, 2021, 105445.

[14] Sajid, M., Ali, N., Javed, T., Abbas, Z., Stretching a curved surface in a viscous fluid, *Chinese Physics Letters*, 27(2), 2010, 024703.

[15] Naveed, M., Abbas, Z., Sajid, M., MHD flow of micropolar fluid due to a curved stretching sheet with thermal radiation, *Journal of Applied Fluid Mechanics*, 9(1), 2015, 131-138.

[16] Sanni, K.M., Asghar, S., Jalil, M., Okechi, N.F., Flow of viscous fluid along a nonlinearly stretching curved surface, *Results in Physics*, 7, 2017, 1-4.

[17] Hayat, T., Sajjad, R., Ellahi, R., Alsaedi, A., Muhammad, T., Homogeneous-heterogeneous reactions in MHD flow of micropolar fluid by a curved stretching surface, *Journal of Molecular Liquids*, 240, 2017, 209-220.

[18] Khan, N.S., Hussanan, A., Kumam, W., Kumam, P., Suttiarporn, P., Accessing the thermodynamics of Walter-B fluid with magnetic dipole effect past a curved stretching surface, *ZAMM-Journal of Applied Mathematics and Mechanics/Zeitschrift für Angewandte Mathematik und Mechanik*, 103(8), 2023, e202100112.

[19] Boyer, T.H., The force on a magnetic dipole, *American Journal of Physics*, 56(8), 1988, 688-692.

[20] Ishak, A., Mixed convection boundary layer flow over a horizontal plate with thermal radiation, *Heat and Mass Transfer*, 46(2), 2009, 147-151.

[21] Zeeshan, A., Majeed, A., Heat transfer analysis of Jeffery fluid flow over a stretching sheet with suction/injection and magnetic dipole effect, *Alexandria Engineering Journal*, 55(3), 2016, 2171-2181.

[22] Usman, A.H., Khan, N.S., Rano, S.A., Maitama, M., Study of heat and mass transfer in MHD flow of Sutter by nanofluid over a curved stretching sheet with magnetic dipole and effect, *Thai Journal of Mathematics*, 19(3), 2021, 1037-1055.

[23] Kumar, P., Nagaraja, B., Almeida, F., AjayKumar, A.R., Al-Mdallal, Q., Jarad. F., Magnetic dipole effects on unsteady flow of Casson-Williamson nanofluid propelled by stretching slippery curved melting sheet with buoyancy force, *Scientific Reports*, 13(1), 2023, 12770.

[24] Hayat, T., Kiran, A., Imtiaz, M., Alsaedi, A., Hydromagnetic mixed convection flow of copper and silver water nanofluids due to a curved stretching sheet, *Results in Physics*, 6, 2016, 904-910.

[25] Hayat, T., Rashid, M., Imtiaz, M., Alsaedi, A., MHD convective flow due to a curved surface with thermal radiation and chemical reaction, *Journal of Molecular Liquids*, 225, 2017, 482-489.

[26] Patel, H.R., Singh, R., Thermophoresis, Brownian motion and non-linear thermal radiation effects on mixed convection MHD micropolar fluid flow due to nonlinear stretched sheet in porous medium with viscous dissipation, joule heating and convective boundary condition, *International Communications in Heat and Mass Transfer*, 107, 2019, 68-92.

[27] Muhammad, K., Hayat, T., Alsaedi, A., Numerical study of Newtonian heating in flow of hybrid nanofluid SWCNTs+CuO Ethylene glycol) past a curved surface with viscous dissipation, *Journal of Thermal Analysis and Calorimetry*, 143, 2021, 1291-1302.

[28] Nagaraja, B., Gireesha. B.J., Exponential space-dependent heat generation impact on MHD convective flow of Casson fluid over a curved stretching sheet with chemical reaction, *Journal of Thermal Analysis and Calorimetry*, 143, 2021, 4071-4079.

[29] Muhammad R., Khan, M.I., Khan, N.B., Jameel, M., Magnetohydrodynamics (MHD) radiated nanomaterial viscous material flow by a curved surface with second order slip and entropy generation, *Computer Methods and Programs in Biomedicine*, 189, 2020, 105294.

[30] Almeida, F., Gireesha, B.J., Venkatesh, P., Nagaraja, B., KKL Model for Magnetized Al203-Nanoliquid Drift in Microchannel Reckoning Brownian Motion, *International Journal of Applied and Computational Mathematics*, 9(6), 2023, 148.

[31] Sakkaravarthi, K., Reddy, P.B.A., Non-linear thermal radiation and entropy generation on MHD Casson and Williamson hybrid nanofluids across a curved stretching sheet with Cattaneo-Christov heat flux model, *Radiation Effects and Defects in Solids*, 179(3-4), 2024, 386-420.

ORCID iD

K.G. Vidhya https://orcid.org/0009-0003-3380-4849
F. Almeida https://orcid.org/0000-0003-2136-8771
P. Kumar https://orcid.org/0000-0002-4875-5387
B. Nagaraja https://orcid.org/0000-0002-8081-9950

How to cite this article: Vidhya K.G., Almeida F., Kumar P., Nagaraja B. Intervention of the Koo-Kleinstreuer and Li Model in Nanofluid Flow over Magnetic Dipole Centered Curved Sheet and Optimizing Entropy using Response Surface Methodology, *J. Appl. Comput. Mech.*, 11(2), 2025, 382-398. https://doi.org/10.22055/jacm.2024.46802.4595